



Extracting inter-particle forces in opaque granular materials: Beyond photoelasticity



Ryan Hurley, Eloïse Marteau, Guruswami Ravichandran, José E. Andrade*

Division of Engineering & Applied Science, California Institute of Technology, Pasadena, CA 91125, USA

ARTICLE INFO

Article history:

Received 18 February 2013

Received in revised form

23 July 2013

Accepted 17 September 2013

Available online 4 October 2013

Keywords:

Granular element method

Contact forces

Discrete mechanics

Multiscale modeling

ABSTRACT

This paper presents the first example of inter-particle force inference in real granular materials using an improved version of the methodology known as the Granular Element Method (GEM). GEM combines experimental imaging techniques with equations governing particle behavior to allow force inference in cohesionless materials with grains of arbitrary shape, texture, and opacity. This novel capability serves as a useful tool for experimentally characterizing granular materials, and provides a new means for investigating force networks. In addition to an experimental example, this paper presents a precise mathematical formulation of the inverse problem involving the governing equations and illustrates solution strategies.

© 2013 Published by Elsevier Ltd.

1. Introduction

Granular materials are ubiquitous in nature and technology: soils, foods, industrial products, and many other natural and engineered materials are granular (Jaeger et al., 1996). Although these materials are governed by seemingly simple laws on the particle scale, their observed mesoscopic and macroscopic behavior is complex and not fully explained by any unified theory. A primary goal in the study of granular materials has therefore been to understand their behavior from a micro-mechanical standpoint using only simple mechanical laws and observations of particle level phenomena.

Significant progress has been made in studying microscopic features of granular materials. Inter-particle forces and force chains have received extensive attention (e.g., Cates et al., 1998; Peters et al., 2005 and references therein). Studies have examined relations between inter-particle forces and bulk properties (Rothenburg and Bathurst, 1989; Bathurst and Rothenburg, 1990). Extensive research has focused on collective statistical properties of inter-particle forces (Majmudar and Behringer, 2005; Coppersmith et al., 1996; Guo and Zhao, 2013; Liu et al., 1995; Ostojic et al., 2006; Radjai et al., 1996, 1998; Satake, 1982). Many models have emerged to simulate the observed heterogeneities of force networks (Bouchaud et al., 2001; Claudin et al., 1998; Liu et al., 1995). Modeling techniques embracing the link between inter-particle forces and macroscopic properties have also emerged and successfully reproduced many observed features of granular materials (Andrade and Tu, 2009; Andrade et al., 2011). The progress and success of these studies hinges on the ability to validate theories with experiments on real granular materials. To this end, experimental techniques for inferring inter-particle forces are essential.

Several experimental techniques have historically provided powerful methods for inferring inter-particle forces in granular materials. Photoelasticity has provided the most popular and widely used technique (Drescher and de Josselin de Jong, 1972; Howell et al., 1999). While photoelasticity has and will continue to occupy an important place in the study

* Corresponding author.

E-mail address: jandrade@caltech.edu (J.E. Andrade).

of granular materials, it has many limitations: it requires the use of birefringent grains with simple geometries, is difficult to implement in three dimensions, and it often requires knowledge of boundary forces for accurate results (Frocht, 1941a,b). Other methods proposed recently attempt to overcome some of these limitations but are also restricted to particular materials or grain shapes (see e.g., Saadatfar et al., 2012; Zhou et al., 2006). For example, Saadatfar et al. (2012), Zhou et al. (2006) are restricted to spherical particles and rely on a particular choice of contact law. As a consequence, the materials of choice have to be relatively soft, e.g., rubber or droplets. Also, the droplets in Zhou et al. (2006) are frictionless. While these methods constitute a great first step in the desired direction, there are still no experiment-based quantitative values of interparticle forces reported in the literature. The methodology presented in this paper leverages emerging experimental techniques to overcome many of these limitations: it can be applied to real, complex materials of arbitrary shape and opacity, is compatible with a number of imaging methods (including x-ray diffraction and tomography), it does not rely on any contact law, and has a simple and physically intuitive mathematical structure.

The Granular Element Method (GEM) presented in this paper is an extended form of the method originally proposed in Andrade and Avila (2012). The contribution of this paper is to present an experimental validation of GEM representing the first application of GEM to infer inter-particle forces in complex opaque materials and to present a precise mathematical formulation of the proposed inverse problem involving the governing equations for particle mechanics. This paper also provides an additional inverse problem formulation that may help to practitioners reduce solution error when experimental noise is present. The contribution of the GEM framework itself is more profound: GEM provides a general framework for inferring inter-particle forces in two or three dimensions and in any granular material, provided that the necessary data can be obtained through experiments.

The GEM methodology can be visualized in Fig. 1. Experimental imaging techniques such as high-resolution photography, 3D X-ray diffraction (Hall et al., 2011; Martins et al., 2004; Poulsen, 2004), and X-ray computed tomography (XRCT) (Alshibili and Reed, 2010; Desrues et al., 2006; Wang et al., 2007) provide rich data sets from which Digital Image Correction (DIC) (Sutton et al., 2009), level-set methods (Vlahinic et al., under review), and other techniques can extract intra-particle strain fields and material fabric (contact locations and normals). Intra-particle strains fields and material fabric are used as input into a mathematical framework which yields intra-particle stress fields using an appropriate constitutive relation and numerically solves an inverse problem using the governing equations of particle statics. The result of the inverse problem is inter-particle forces, a key component in the development of theories regarding granular behavior. Because GEM can be coupled with any experimental techniques capable of extracting strain fields and fabric, recent advances in imaging (e.g., Hall et al., 2011; Martins et al., 2004) will soon allow inference of inter-particle forces in natural materials with small grains, such as sands.

The layout of this paper is as follows. Section 2 presents an example of the methodology applied to a real experiment involving rubber particles, showcasing the applicability of the method to real materials of any texture and its adaptability to a number of experimental imaging and algorithmic data analysis techniques. Sections 3 and 4 detail the ingredients of the mathematical framework of GEM. Section 5 illustrates additional features of GEM with a numerical example. Finally, Section 6 offers concluding remarks.

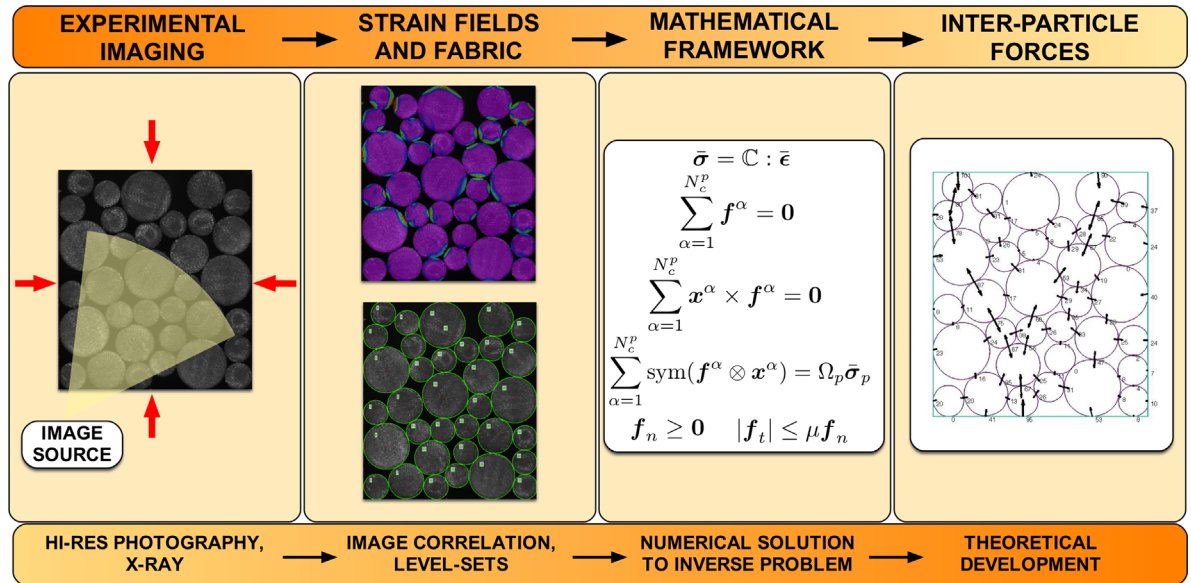


Fig. 1. The GEM methodology for inter-particle force-inference presented in this paper. Experimental imaging techniques provide rich data sets for extracting intra-particle strain fields and material fabric. These ingredients are input into a mathematical framework which yields inter-particle forces by solving an appropriate inverse problem. Variables and equations in panel 3 are described in Section 3.

The notation and terminology used in this paper are defined as follows: $\mathbb{R}^{m \times n}$ denotes the set of real matrices with m rows and n columns, “ \cdot ” denotes an inner product (e.g. $\mathbf{a} \cdot \mathbf{b} = a_i b_i$; $\mathbf{c} \cdot \mathbf{d} = c_{ij} d_{jk}$), “ \otimes ” denotes a dyadic product (e.g. $\mathbf{a} \otimes \mathbf{b} = a_i b_j$), $\|\cdot\|_2$ denotes the Euclidian norm of a vector (e.g., $\|\mathbf{a}\|_2 = \sqrt{a_1^2 + \dots + a_n^2}$), and “sym” is the symmetric operator defined as $\text{sym}(\cdot) = 1/2((\cdot) + (\cdot)^T)$. $\mathcal{R}(\mathbf{A})$ refers to the range of \mathbf{A} , the set of all possible linear combinations of the columns of \mathbf{A} . $\mathcal{N}(\mathbf{A})$ refers to the nullspace of \mathbf{A} , the set of all vectors \mathbf{z} such that $\mathbf{A}\mathbf{z} = \mathbf{0}$.

2. Experimental validation and application of GEM

This section presents an example of GEM applied to a real experiment. The current experiment uses Digital Image Correlation (DIC) to measure full-field particle strains from which stresses are deduced. Information about the location of contact points and particle shapes are obtained from digital images using segmentation algorithms. This data is then passed to the GEM algorithm, which reconstructs the force distribution. The results of this experiment showcase the applicability of GEM to real materials and its potential to be combined with advanced experimental techniques.

2.1. Experimental setup and procedure

The experimental setup is shown in Fig. 2. A CMOS camera with a 3.0 megapixel sensor (PL-B623, PixeLINK, Ottawa, Canada) and a Canon lens was used at a working distance of 20 cm to image the assembly. A specifically designed loading device is used to apply axial compression on the specimen, as shown in Fig. 2. The specimen is placed between four faces: the bottom and lateral faces are stationary and the top face can move vertically. The applied force was carefully measured with a 500 g load cell (LCFA-50G, Omega, Stamford, CT) and monitored with a digimeter (MD-40, Newport, Irvine, CA).

The specimen used in the experiment was composed of rubber cylindrical grains. Grain diameters were 7 mm, 10 mm, or 14 mm, and the grains' out-of-plane length was 20 mm. The grains' Young's modulus was 5.5 MPa and Poisson's ratio was approximately 0.5. The specimen shown in Fig. 3 was compressed with a 215 N vertical load on the top wall, while the side walls were held rigid.

The software VIC-2D was used to perform Digital Image Correlation (DIC) on the images in order to determine in plane full-field strain ([Correlated Solutions. Vic-2D, Reference Manual](#); [Correlated Solutions. Vic-2D, Testing Guide](#)). Digital Image Correlation (DIC) is an optical tool based on digital image processing and numerical computing which provides full-field displacements and strains by comparing the gray intensity changes of the object surface before and after deformation ([Pan et al., 2009](#); [Sutton et al., 2009](#)). The DIC procedure consists of tracking the same pixels between reference and deformed images. To perform this tracking, a correlation window, or subset, is chosen and deformed until the pattern in the deformed image matches the pattern in the reference image as closely as possible. To determine an adequate subset size, a compromise between resolution and measurement error needs to be found. The measurement error is evaluated by correlating two subsequent images of the specimen without applying any deformation. The values of the resulting strain components (ϵ_{xx} , ϵ_{yy} and ϵ_{xy}) for different subset sizes are then compared in order to identify suitable configurations. The degree of similarity between the reference and deformed subsets is computed using a correlation coefficient and the best fit is achieved when the correlation coefficient reaches its maximum. The position of the deformed subset is determined and the in-plane displacement is obtained by calculating the difference between the position of each point in the reference subset and the position of the corresponding point in the deformed subset. The strain field is then computed by numerical differentiation of the displacement field.

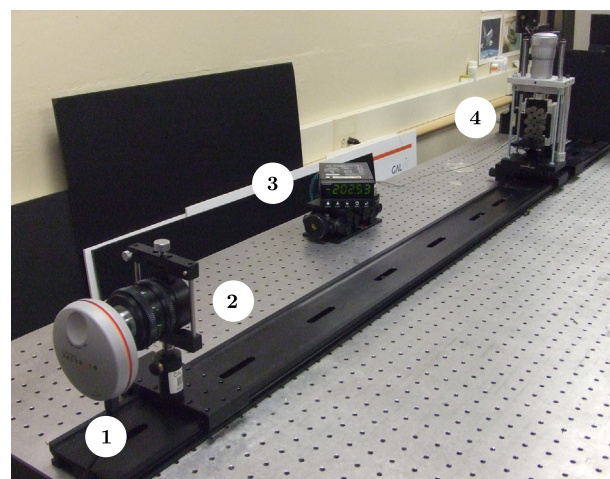


Fig. 2. Experimental setup: 1. CMOS camera; 2. Canon lens; 3. Digimeter; 4. Loading device.

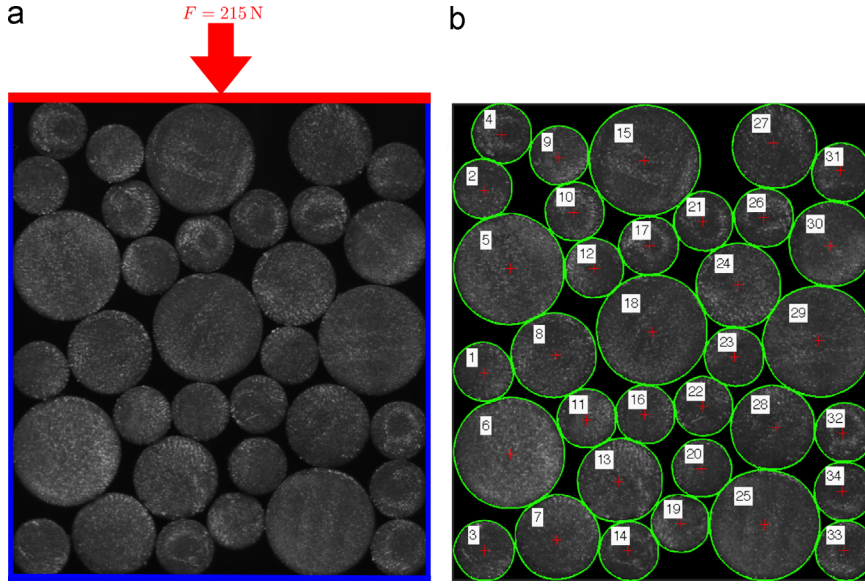


Fig. 3. (a) Sample under macroscopic loading. Top face (red) was prescribed a vertical load of 215 N using a smooth, rigid wall. Bottom and lateral faces (blue) were smooth, stationary walls. (b) Results of segmentation process. (For interpretation of the references to color in this figure caption, the reader is referred to the web version of this paper.)

Segmentation algorithms were used to extract the material's fabric: particle contact points, centroids and areas. In particular, a circular Hough transform (Ballard, 1981; Peng, 2010) was first performed to determine the number of particles N_p , approximate positions of centroids and maximum radii, followed by a snake, or active contour model algorithm (Kass et al., 1988; Kroon, 2011) to determine the true contours of the grain. The different parameters of the Hough transform and active contour model algorithm are manually adjusted by visual inspection of the resulting segmentation of the grains. Segmentation is finally achieved by partitioning the digital images into sets of pixels, each set constituting different particles. The result of this segmentation procedure is shown in Fig. 3.

2.2. Strain fields and force results

The contact locations, particle areas and average particle strain, were used as input into GEM's mathematical framework to be described in Sections 3 and 4.

A simple algorithm was used to determine the position of the contact points. First, grain boundaries were delineated as shown in Fig. 3. Next, the euclidean distance between pixels on two adjacent boundaries was calculated and the two pixels were considered to belong to a contact surface if this distance was less than or equal to a certain pixel threshold L_{pix} . Finally, the average value of positions of all pixels belonging to a contact surface was used to determine a single coordinate (x, y) of the true contact point. The results of this algorithm are shown in Fig. 4, where it can be seen that the 34 particles share a total of 78 contact points.

Fig. 5 shows the full-field strain distribution obtained from DIC. The DIC procedure was applied grain by grain. For each grain, the subset size was manually chosen in order to achieve a reliable correlation analysis. The full-field strain distribution was obtained by calculating values of ε_{xx} , ε_{yy} and ε_{xy} inside of each particle using numerical differentiation of the displacement field. The average strain tensor, $\bar{\varepsilon}^p$, was obtained by taking the arithmetic average of each tensor computed within a given particle. The average stress $\bar{\sigma}^p$ of a particle was deduced from the average strain $\bar{\varepsilon}^p$ using generalized Hooke's law, $\bar{\sigma}^p = \mathbf{c} : \bar{\varepsilon}^p$, where $\bar{\sigma}^p$ is the average elastic stress tensor at a particle and \mathbf{c} is the elastic stiffness tensor of the particle. The Young's modulus and Poisson's ratio used in the elastic stiffness tensor were determined using a separate experiment on a single grain.

Using average particle strain and fabric information, the regularized inverse problem in Eq. (14) was solved with a regularization parameter of $\lambda = 0.0024$. The resulting inter-particle forces are shown in Fig. 6. It should be emphasized that the presented forces are forces distributed over the length of the cylinder. Fig. 6 offers the first look at inter-particle forces inferred in a real, opaque material using GEM. The forces form expected patterns of force chains throughout the material. The particle–boundary forces along the top platen were measured by the load cell to be 215 N and the calculated resultant forces sum to 215 N.

The average macroscopic stress in the array was also computed using the expression (Christoffersen et al., 1981)

$$\langle \sigma \rangle = \frac{1}{\Omega} \sum_{\alpha=1}^{N_c} \text{sym}(\mathbf{f}^\alpha \otimes \mathbf{d}^\alpha) \quad (1)$$

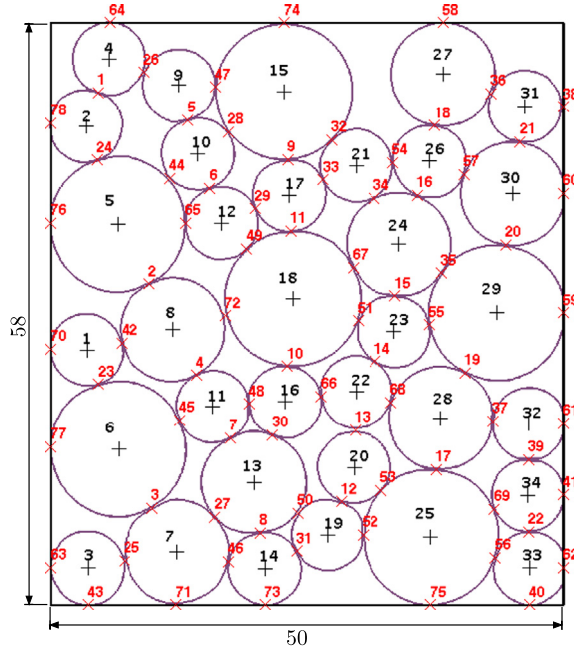


Fig. 4. Sample dimensions in millimeters and information on the fabric: particle numbers, position of contact points and centroids.

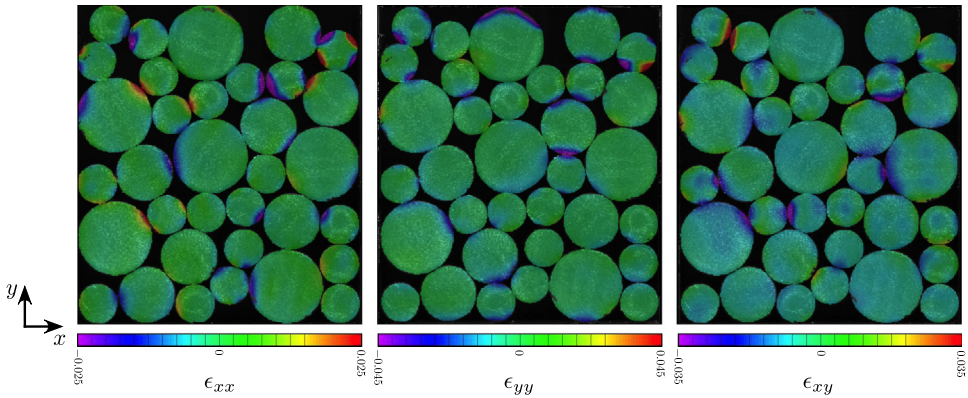


Fig. 5. Strain components ϵ_{xx} , ϵ_{yy} and ϵ_{xy} obtained from DIC.

where Ω is the volume of the assembly, N_c is the number of inter-particle contacts in the assembly, $\langle \sigma \rangle$ is the macroscopic average stress, \mathbf{f}^a is the inter-particle contact force, and \mathbf{d}^a is the branch vector between particles. The resulting macroscopic stress was computed to be

$$\langle \sigma \rangle = \begin{bmatrix} -2.56 & 0.26 \\ 0.26 & -4.42 \end{bmatrix} \text{ (kPa)} \quad (2)$$

where compressional stresses are negative. The $\langle \sigma \rangle_{22}$ component of this result corresponds well with the applied stress of $-215 \text{ N}/0.05 \text{ m} = -4.3 \text{ kPa}$, a motivational result considering that Eq. (1) is approximate since branch vectors between particles and walls were not included.

The result of this experiment underscores the power of GEM for inferring inter-particle forces in real opaque materials. The experiment also illustrates the versatility of GEM: it is adaptable to any experimental technique able to furnish the required input. The following sections describe GEM's mathematical framework in more detail and describe precisely how the required ingredients are used to produce inter-particle force estimates.

3. Governing equations

This section describes the equations governing particle behavior in cohesionless granular materials in static equilibrium. Underlying the formulation of all governing equations is the assumption of point contact. This assumption is valid for many

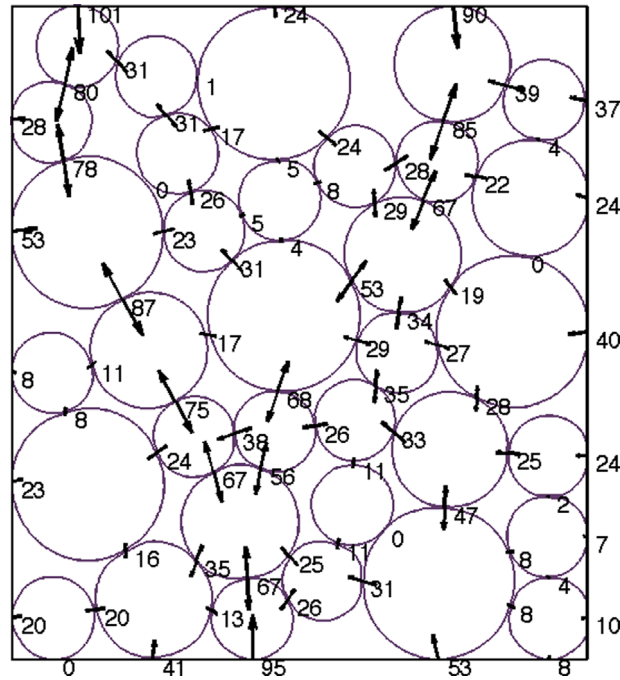


Fig. 6. Resulting inter-particle forces (in N) from application of GEM.

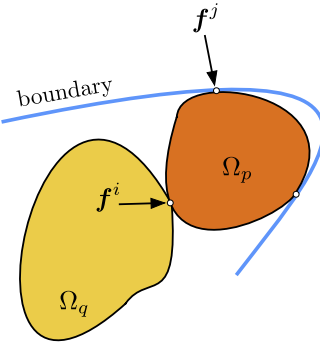


Fig. 7. Illustration of particle-particle and particle-boundary contacts.

stiff particles of interest in granular physics, including, for instance, sands, powders, and many pharmaceuticals. In the case of more compliant particles, this approximation may remain accurate for moderate load levels.

3.1. Equilibrium

Consider the p th particle in a static granular material, interacting with other particles through N_c^p contact points labeled with index α (see Fig. 7). Balance of forces and moments yields the two equilibrium equations:

$$\sum_{\alpha=1}^{N_c^p} \mathbf{f}^\alpha = \mathbf{0} \quad (3)$$

$$\sum_{\alpha=1}^{N_c^p} \mathbf{x}^\alpha \times \mathbf{f}^\alpha = \mathbf{0} \quad (4)$$

where \mathbf{x}^α is a vector from a conveniently chosen origin to the contact point α , and \mathbf{f}^α is a force vector acting at α .

Eqs. (3) and (4) can be combined into a single matrix expression for an entire assembly of particles: $\mathbf{K}_{eq}\mathbf{f} = \mathbf{0}$. In two dimensions, the system takes the form

$$\begin{matrix} i & j \\ \begin{matrix} p \\ q \end{matrix} & \begin{bmatrix} \ddots & \mathbf{0} & \cdots & \mathbf{0} & \cdots \\ \mathbf{0} & \mathbf{K}_{eq}^i & \mathbf{0} & \mathbf{K}_{eq}^j & \mathbf{0} \\ \vdots & \mathbf{0} & \ddots & \mathbf{0} & \vdots \\ \mathbf{0} & -\mathbf{K}_{eq}^i & \mathbf{0} & \mathbf{0} & \mathbf{0} \\ \vdots & \mathbf{0} & \vdots & \mathbf{0} & \ddots \end{bmatrix} & \begin{pmatrix} \vdots \\ \mathbf{f}^i \\ \vdots \\ \mathbf{f}^j \\ \vdots \end{pmatrix} = \begin{pmatrix} \vdots \\ \mathbf{0} \\ \vdots \\ \mathbf{0} \\ \vdots \end{pmatrix}; \quad \mathbf{K}_{eq}^i = \begin{bmatrix} 1 & 0 \\ 0 & 1 \\ -x_2^i & x_1^i \end{bmatrix}; \quad \mathbf{f}^i = \begin{pmatrix} f_1^i \\ f_2^i \end{pmatrix} \end{matrix} \quad (5)$$

where p and q represent particles, i and j represent particle-particle and particle-boundary contacts as shown in Fig. 7.

The extension to three dimensions is straightforward and omitted for brevity. In general, \mathbf{K}_{eq} will have $dN_p(d+1)/2$ rows and dN_c columns where d is the dimension (e.g., $d=2$ for 2D), N_p is the total number of particles in the assembly and N_c is the total number of contact points in the assembly.

3.2. Average particle stress

The average Cauchy stress for a particle in equilibrium under the action of discrete boundary forces can be derived by considering the volume averaged stress equation for a particle p

$$\bar{\sigma}^p = \frac{1}{\Omega_p} \int_{\Omega_p} \sigma^p \, dv \quad (6)$$

where Ω_p indicates integration over the deformed volume (in 3D) or area (in 2D) of the particle p . By considering balance of linear momentum, the divergence theorem, and the symmetry of the Cauchy stress tensor, this expression takes the form (see Andrade and Avila, 2012 for more details)

$$\bar{\sigma}^p = \frac{1}{\Omega_p} \sum_{\alpha=1}^{N_c^p} \text{sym}(\mathbf{f}^\alpha \otimes \mathbf{x}^\alpha) \quad (7)$$

Eq. (7) can be written in matrix form for an entire assembly of particles as $\mathbf{K}_{st}\mathbf{f} = \mathbf{b}_{st}$. In two dimensions, the system takes the form

$$\begin{matrix} i & j \\ \begin{matrix} p \\ q \end{matrix} & \begin{bmatrix} \ddots & \mathbf{0} & \cdots & \mathbf{0} & \cdots \\ \mathbf{0} & \mathbf{K}_{st}^i & \mathbf{0} & \mathbf{K}_{st}^j & \mathbf{0} \\ \vdots & \mathbf{0} & \ddots & \mathbf{0} & \vdots \\ \mathbf{0} & -\mathbf{K}_{st}^i & \mathbf{0} & \mathbf{0} & \mathbf{0} \\ \vdots & \mathbf{0} & \vdots & \mathbf{0} & \ddots \end{bmatrix} & \begin{pmatrix} \vdots \\ \mathbf{f}^i \\ \vdots \\ \mathbf{f}^j \\ \vdots \end{pmatrix} = \begin{pmatrix} \vdots \\ \mathbf{b}_{st}^p \\ \vdots \\ \mathbf{b}_{st}^q \\ \vdots \end{pmatrix}; \quad \mathbf{K}_{st}^i = \begin{bmatrix} x_1^i & 0 \\ 0 & x_2^i \\ x_2^i & x_1^i \end{bmatrix}; \quad \mathbf{b}_{st}^p = \begin{bmatrix} \Omega_p \bar{\sigma}_{11}^p \\ \Omega_p \bar{\sigma}_{22}^p \\ 2\Omega_p \bar{\sigma}_{12}^p \end{bmatrix} \end{matrix} \quad (8)$$

Extension to 3D is again straightforward and is omitted for brevity. Similar to \mathbf{K}_{eq} , the matrix \mathbf{K}_{st} has $dN_p(d+1)/2$ rows and dN_c columns, where d is the dimension (e.g., $d=2$ for 2D), N_p is the total number of particles in the assembly and N_c is the total number of contact points in the assembly.

3.3. Cohesionless and tangential forces

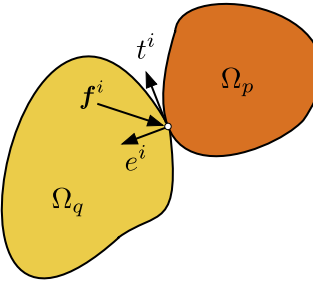
Cohesion-less granular materials in equilibrium obey two additional laws: normal forces are repulsive and tangential forces are governed by a Coulomb type friction law. The latter constraint requires that $|f_t| \leq \mu |f_n|$, where f_t is a tangential force magnitude, f_n is a corresponding normal force magnitude, and μ is the inter-particle coefficient of friction. These two constraints can be written for any contact point acting on the p th particle as

$$-\mathbf{e}^i \cdot \mathbf{f}^i \geq 0 \quad (9)$$

$$-\left(\mathbf{e}^i + \frac{1}{\mu} \mathbf{t}^i\right) \cdot \mathbf{f}^i \geq 0 \quad (10)$$

$$-\left(\mathbf{e}^i - \frac{1}{\mu} \mathbf{t}^i\right) \cdot \mathbf{f}^i \geq 0 \quad (11)$$

where \mathbf{e}^i and \mathbf{t}^i represent normal and tangential unit vectors at the contact point i for a particular particle Ω_p , as shown in Fig. 8.

**Fig. 8.** Unit vectors for contact i .

Eqs. (9)–(11) can be combined into a single matrix expression for an entire assembly of particles: $\mathbf{B}\mathbf{f} \geq \mathbf{0}$. In 2D, the system takes the form

$$\begin{array}{ccccc}
 i & i & j & j \\
 \begin{matrix} i \\ j \\ i \\ j \\ i \\ j \\ i \\ j \end{matrix} & \left[\begin{array}{ccccc}
 -e_1^i & -e_2^i & 0 & 0 & 0 \\
 0 & 0 & \ddots & 0 & 0 \\
 0 & 0 & 0 & -e_1^j & -e_2^j \\
 -e_1^i - \frac{1}{\mu}t_1^i & -e_2^i - \frac{1}{\mu}t_2^i & 0 & 0 & 0 \\
 0 & 0 & \ddots & 0 & 0 \\
 0 & 0 & 0 & -e_1^j - \frac{1}{\mu}t_1^j & -e_2^j - \frac{1}{\mu}t_2^j \\
 -e_1^i + \frac{1}{\mu}t_1^i & -e_2^i + \frac{1}{\mu}t_2^i & 0 & 0 & 0 \\
 0 & 0 & \ddots & 0 & 0 \\
 0 & 0 & 0 & -e_1^j + \frac{1}{\mu}t_1^j & -e_2^j + \frac{1}{\mu}t_2^j
 \end{array} \right] & \begin{pmatrix} f_1^i \\ f_2^i \\ \vdots \\ f_1^j \\ f_2^j \\ \vdots \\ f_1^i \\ f_2^i \end{pmatrix} & \geq & \begin{pmatrix} 0 \\ 0 \\ \vdots \\ 0 \\ 0 \end{pmatrix} \quad (12)
 \end{array}$$

where subscripts refer to vector components and superscripts refer to particular contact points. Extension to 3D is straightforward and is omitted for brevity. In general, $\mathbf{B} \in \mathbb{R}^{3N_c \times dN_c}$.

3.4. Structure of equations and connection to experiments

The three matrix equations detailed in this section encapsulate equilibrium relations, constitutive relations, and contact laws for each particle in a granular material in terms of the unknown force components. When the sum of the number of linearly independent rows in both \mathbf{K}_{st} and \mathbf{K}_{eq} exceeds the number of columns in one of these matrices, there are more equations than unknown force components. Furthermore, when \mathbf{K}_{eq} has more linearly independent columns than rows, $\mathbf{K}_{eq}\mathbf{f} = \mathbf{0}$ has an infinite number of solutions and forces can be inferred using the inverse problem formulation detailed in Section 4. In many practical examples of interest, these conditions will be met as indicated by observed coordination numbers in stable static granular packings (Santamarina et al., 2001).

Experimentally measured quantities are required input to the three matrix equations (5), (8), and (12). These quantities can be measured with any suitable procedure and the structure of the equations will remain unchanged. In particular, the matrices \mathbf{K}_{st} , \mathbf{K}_{eq} , and \mathbf{B} contain contact locations and normal and tangent vectors to each contact plane, which can be extracted from experiments using high-resolution photography or X-ray techniques in connection with DIC or level-set methods. Friction coefficients in \mathbf{B} can be estimated using existing literature or experiments. Finally, the vector \mathbf{b}_{st} contains particle areas (or volumes) and average particle stresses. Particle areas (or volumes) can be extracted using image (or data) processing techniques. Particle stresses can be determined by first extracting strain fields using DIC or other algorithms, and then by applying a suitable constitutive relation. Because the mathematical framework incorporates only a single dataset corresponding to one instant in time, it does not currently allow for history dependent constitutive relations and therefore requires a linear or nonlinear elastic relation.

4. Mathematical framework

This section presents the inverse problem formulation for inferring inter-particle forces using the equations $\mathbf{K}_{eq}\mathbf{f} = \mathbf{0}$, $\mathbf{B}\mathbf{f} \geq \mathbf{0}$, and $\mathbf{K}_{st}\mathbf{f} = \mathbf{b}_{st}$.

4.1. Inverse problem formulation

When the conditions discussed in Section 3.4 are satisfied, the unknown force components can be inferred by satisfying equilibrium precisely, and minimizing an L_2 -norm cost function involving forces and average particle stresses

$$\mathbf{f} = \arg \min_{\mathbf{f}} \|\mathbf{K}_{st}\mathbf{f} - \mathbf{b}_{st}\|_2 \quad (13a)$$

$$\text{subject to : } \mathbf{K}_{eq}\mathbf{f} = \mathbf{0} \quad (13b)$$

$$\mathbf{B}\mathbf{f} \geq \mathbf{0} \quad (13c)$$

The L_2 -norm cost function (13a) is typical in inverse problems and represents only one possible cost function for force-inference. In theory, the mathematical framework may be extended to incorporate other cost functions when the structure of noise in \mathbf{b}_{st} (or in other variables) is well known. In general, however, this noise cannot be easily characterized for all possible experimental techniques adaptable to GEM, and in fact is very difficult to characterize even for a single procedure such as DIC (e.g., see Bornert et al., 2009). Therefore, use of the L_2 -norm cost function is retained in the present paper as an example of a method with simple interpretation and implementation, and simple conditions for existence and uniqueness, but not as the only possible method. The inverse problem formulation in Eq. (13) has been reliable in all practical implementations by the authors.

It is important to note that the constraint in Eq. (13c) is not needed in most cases to obtain an accurate solution. In fact, this constraint is unnecessary and does not influence the solution obtained using Eq. (13) except when significant noise is present in experimental measurements. In the case when such noise is present, the constraint (13c) plays the role of ensuring that the selected solution is physically admissible since noise may bias the result towards a force distribution with unrealistically high tangential to normal force ratios or attractive contact forces. The constraint (13c) can also be modified to eliminate the dependence on Coulomb friction when a Coulomb friction law is unjustified or when the friction coefficient cannot be estimated. When Coulomb friction is abandoned, the restriction will only require that normal forces be repulsive.

Conditions for the existence and uniqueness of solution to Eq. (13) are easy to understand. It must be emphasized, however, that existence and uniqueness of a solution to Eq. (13) does not imply that the solution corresponds to the true inter-particle forces but rather to a solution that minimizes the error between experimental observations and calculations made with the governing equations of the problem in an L_2 -norm sense.

Let $\mathcal{S} = \{\mathbf{f} | \mathbf{K}_{eq}\mathbf{f} = \mathbf{0}, \mathbf{B}\mathbf{f} \geq \mathbf{0}\}$, the set of force vectors that satisfy the constraints (13b) and (13c). A solution to (13) exists when \mathcal{S} is nonempty since the cost function in (13a) is bounded below by 0, e.g., when \mathbf{K}_{st} is positive semi-definite. Furthermore, \mathcal{S} is nonempty when \mathbf{K}_{eq} has more columns than rows, and when $\mathbf{B}\mathbf{f} \geq \mathbf{0}$ is solvable, which can be ensured in practice by choosing μ conservatively. The solution is unique if there is no $\mathbf{w} \neq \mathbf{0}$ such that $\mathbf{w} \in \mathcal{N}(\mathbf{K}_{st}) \cap \mathcal{N}(\mathbf{K}_{eq})$ (see proof and other conditions in Theorem 1 of Lötstedt, 1983); such a \mathbf{w} could be added to any existing solution without changing the value of the cost function in (13a) or violating the equality (13b).

From a physical perspective, such a \mathbf{w} is unlikely to exist: nonzero forces in $\mathcal{N}(\mathbf{K}_{st})$ satisfy $\mathbf{K}_{st}\mathbf{f} = \mathbf{0}$ and must cause rigid body particle motion while forces in $\mathcal{N}(\mathbf{K}_{eq})$ satisfy $\mathbf{K}_{eq}\mathbf{f} = \mathbf{0}$ and must result in equilibrium. When \mathbf{K}_{eq} and \mathbf{K}_{st} are rank deficient, such a \mathbf{w} may exist and additional criteria must be satisfied to ensure uniqueness; namely, the $\mathbf{w} \in \mathcal{N}(\mathbf{K}_{st}) \cap \mathcal{N}(\mathbf{K}_{eq})$ must violate the restrictions of constraint (13c) to ensure that the solution to (13) remains unique. It is merely stated here that the authors have never found such a \mathbf{w} to exist in both numerical simulations and experiments, ensuring the uniqueness of solution to (13).

4.2. Measurement noise and alternative formulation

Experimental imaging techniques contain error, or measurement noise. In addition, algorithms used to extract strain fields, contact locations, contact planes, and constitutive law parameters introduce noise. This noise manifests itself in the matrices \mathbf{K}_{eq} , \mathbf{K}_{st} , and \mathbf{B} and in the vector \mathbf{b}_{st} . While high-fidelity imaging can typically ensure negligibly small error in the point-wise quantities used to populate \mathbf{K}_{eq} , \mathbf{K}_{st} , and \mathbf{B} , the vector \mathbf{b}_{st} requires accurate estimation of the particle constitutive model and associated parameters, and involves a sum over all point-wise measured stresses in a particle, potentially introducing significant error.

To account for the possibility of significant measurement error in \mathbf{b}_{st} a simple alternative to the inverse problem (13) is proposed which incorporates knowledge of boundary forces, quantities that are typically found by using load cells in experiments. The alternative method is motivated by the experience that when the solution to (13) is affected by measurement error in the constitutive law, the relative sizes of forces remains relatively unchanged (i.e., all forces are generally over- or underestimated). The alternative inverse problem is given by

$$\mathbf{f} = \arg \min_{\mathbf{f}} \|\mathbf{K}_{st}\mathbf{f} - \mathbf{b}_{st}\|_2 + \lambda^2 \|\mathbf{f}\|_2 \quad (14a)$$

$$\text{subject to : } \mathbf{K}_{eq}\mathbf{f} = \mathbf{0} \quad (14b)$$

$$\mathbf{B}\mathbf{f} \geq \mathbf{0} \quad (14c)$$

where λ is a regularization parameter, to be discussed.

Problem (14) employs Tikhonov regularization, a common technique in the solution of ill-posed or rank-deficient inverse problems (e.g., Hansen, 1995; Vogel, 2002). Tikhonov regularization can be interpreted as a method for incorporating prior knowledge of the magnitude of f and as a technique for selecting a “smoother” solution. This can be seen intuitively: as λ is increased, the solution will decrease until each value of f approaches 0. Furthermore, the solution will typically decrease with some uniformity in that each value of f will approach 0 at a rate proportional to its size. It is important to note, however, that the solution to problem (14) will still satisfy particle equilibrium.

The primary challenge in using the alternative form (14) is selecting λ to find a tradeoff between noise reduction and loss of information (Vogel, 2002). When the structure of noise in \mathbf{b}_{st} is well known, many methods exist to select λ , although all methods have known issues and limitations (Bauer and Lukas, 2011). The technique used in this paper to select λ is simple and has been proven effective by experience: gradually increase λ until a solution \mathbf{f} to (14) minimizes the difference between known and calculated boundary forces. Example of implementing this procedure is presented in the next section and the experimental example in Section 2. In general, the mathematical framework presented in this section may be extended to incorporate penalty functions other than Tikhonov regularization, but it is beyond the scope of this paper to address all of these possibilities. It is important to note that solution of Eq. (14), as with the solution of Eq. (13), will produce forces that satisfy particle equilibrium.

4.3. Implementation

Many solvers and optimization packages exist to solve the minimization problem (13) or (14). In particular, implementations of SeDuMi (Sturm, 1999) such as CVX (Grant and Boyd, 2011) and Yalmip (Lofberg, 2004) provide efficient ways to solve the problem in Matlab. In addition, any numerical optimization package capable of solving quadratic programming problems can be used to solve (13) and (14) when the cost functions in these problems are expanded to quadratic form (e.g.: $\min\{f^T K_{st}^T K_{st} f - 2b^T K_{st} f\}$). Since the matrices K_{eq} and K_{st} may not be full rank in practice, solvers capable of handling rank deficient matrices may be preferred.

5. Numerical example

This section presents a numerical example of implementing GEM. This example is used to demonstrate the salient features of the method in an environment where the exact solution, or exact inter-particle forces are known. A metric used throughout this example is relative error, $\|\delta f\|$, defined as

$$\|\delta \mathbf{f}\| = \frac{\|\mathbf{f}^{\text{Calculated}} - \mathbf{f}^{\text{Actual}}\|}{\|\mathbf{f}^{\text{Actual}}\|} \quad (15)$$

To generate a suitable data set for demonstrating the features of GEM, an odometric compression test was performed on a rectangular sample of 58 particles using the Discrete Element Method (DEM) ([Cundall and Strack, 1979](#)). The particle radii were uniformly distributed between 2.5 mm and 4 mm. The particle–particle and particle–wall coefficients of friction were 0.5 and 0, respectively. No gravity acted on the particles. The normal and tangential stiffnesses were 67.5 KN/mm. The applied compressive stress was 30 kPa on the top face, as shown in [Fig. 9](#).

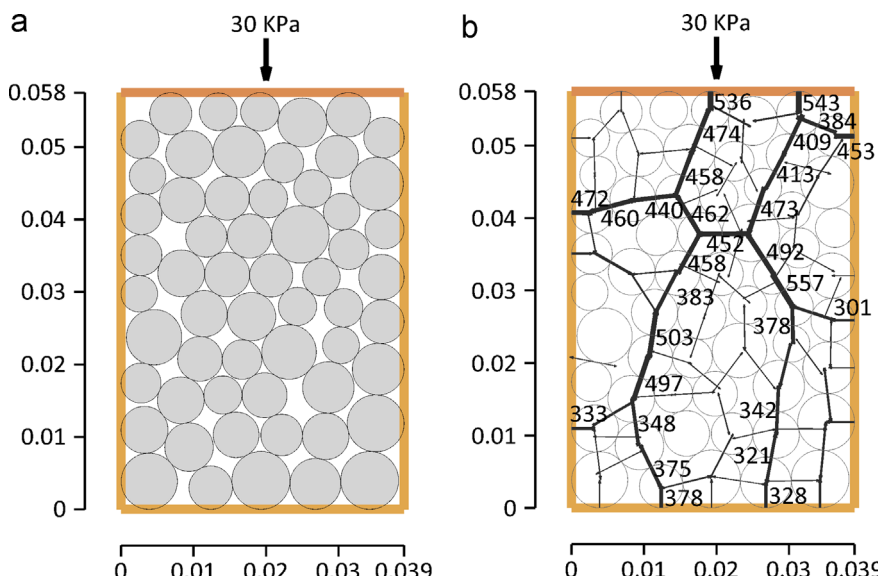


Fig. 9. (a) Numerical odometric test setup. (b) Inter-particle forces computed with DEM and (13). Length scale in meters, forces in Newtons. Line thickness proportional to force magnitude.

5.1. Global force inference

After the DEM simulation neared an equilibrium state, contact forces, normal and tangential contact vectors, and average particle stresses determined by Eq. (7) were used to form the matrices \mathbf{K}_{st} , \mathbf{K}_{eq} , \mathbf{B} , and the vector \mathbf{b}_{st} . The inter-particle friction coefficient for all contacts was assumed to be 0.5. The problem (13) was solved and the exact inter-particle forces were recovered with relative error, $\|\delta\mathbf{f}\| \approx 0$. Since forces from DEM exactly matched those found using (13), the forces are plotted only once in Fig. 9. Only forces with magnitude over 300 N are labeled.

5.2. Noise reduction

To demonstrate the application of the modified inverse problem (14), noise was added to each element of \mathbf{b}_{st} as follows: each element was first increased by 15% to simulate overestimating the Young's modulus in a linearly elastic constitutive model, and then each element was added to the product of its original value with a unique number generated from a Gaussian distribution with mean 0 and standard deviation 0.1 to simulate noise generated from image resolution and strain field calculation algorithms. Each element of the new \mathbf{b}_{st} therefore took the form

$$(\mathbf{b}_{st})_i = (\mathbf{b}_{st})_i + (0.15 + N(0, 0.1))(\mathbf{b}_{st})_i \quad (16)$$

where $N(0, 0.1)$ represents a number generated from a Gaussian distribution with mean 0 and standard deviation 0.1.

Problem (13) was first solved, yielding results with $\|\delta\mathbf{f}\| = 0.154$ as shown in Fig. 10. Despite the noticeable differences between the forces in Fig. 10 and the exact forces, the solution in Fig. 10 does not violate Coulomb friction by virtue of the inequality constraints used in the optimization problem (13).

Next, problem (14) was solved, yielding results with $\|\delta\mathbf{f}\| = 0.053$ as shown in Fig. 10. The total force on the top boundary measured from the DEM simulation was approximately 1170 N. The regularization parameter λ was chosen to minimize the difference between this value and the sum of the particle–boundary reaction forces on the top boundary

$$\text{Total Difference} = \left| 1170 + \sum_{\alpha}^{N_c^b} f_2^{\alpha} \right| \quad (17)$$

where N_c^b is the number of contact points on the top boundary and f_2^{α} is the vertical component of force acting at contact points along the top boundary. A value of $\lambda = 0.0714$ was found to minimize this total difference by solving (14) with a variety of values over an interval between 0.06 and 0.075.

From the reduced relative error and a qualitative comparison of Figs. 9 and 10, it is clear that the formulation in Eq. (14) significantly improved the accuracy of the solution to the inverse problem. The effect of overestimating Young's modulus was nearly eliminated and the relative error was reduced to levels more representative of the Gaussian noise alone. Other numerical examples not presented here demonstrate the same capability with other forms of artificial measurement noise. This alternative formulation of the inverse problem represents an important extension of GEM for practitioners, providing a means for obtaining solutions with higher accuracy. It is important to note, however, that this method is largely based on judgment: selection of λ is an interactive process, particularly when using the method of minimizing a non-convex function like the total difference in (17).

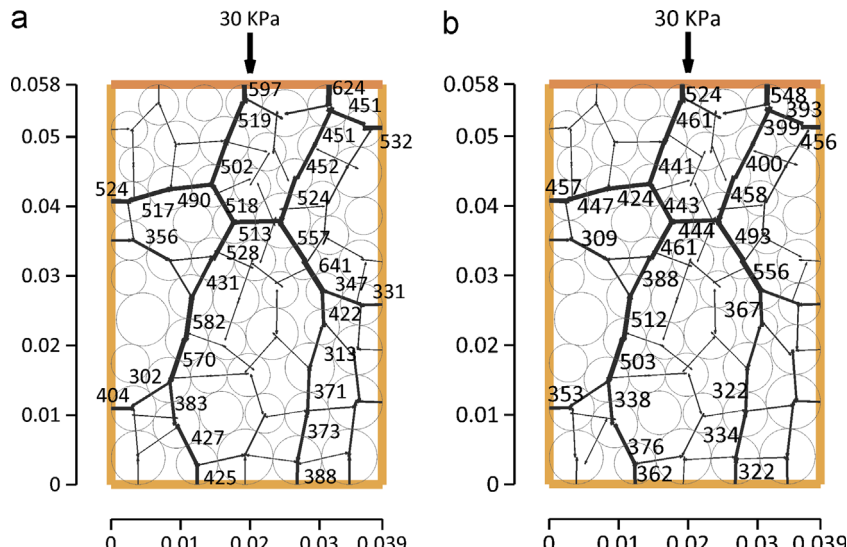


Fig. 10. (a) Solution to (13) with artificial noise, $\|\delta\mathbf{f}\| = 0.154$. (b) Solution to (14) with same noise, $\|\delta\mathbf{f}\| = 0.053$ (right).

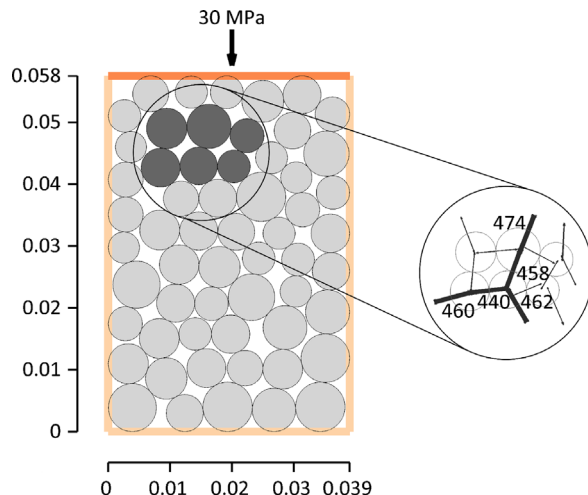


Fig. 11. Solution to (13) performed locally within granular material.

5.3. Local force inference

The proposed formulation in Eq. (13) has the capability of extracting forces locally within a material. To demonstrate this capability, force inference was performed on 6 particles, as shown in Fig. 11. The contact points, corresponding normal and tangent vectors, and average particle stresses for these particles only were used to form the quantities K_{st} , K_{eq} , b_{st} , and B . The contact forces were inferred using (13). Comparison with Fig. 9 shows that the inferred local contact forces exactly match those from the DEM simulation.

The capability of the proposed method to infer contact forces locally represents an important feature of GEM. This feature allows force inference in regions of interest (e.g., shear bands) without the necessity of solving an inverse problem for the entire assembly. Furthermore, this feature may allow GEM to be used in connection with larger experiments since only a small portion of the material's fabric needs to be imaged and processed.

6. Conclusion

The improved formulation of GEM presented in this paper provides a powerful methodology for investigating inter-particle forces in granular materials. The first experimental example using GEM has been showcased to demonstrate that the method can and has been applied to real materials. The presentation of the mathematical framework illustrates its simplicity and versatility, and offers many possibilities of extending the framework to incorporate additional experimental measurements such as boundary forces. With progress in experimental imaging and intra-particle strain field extraction (e.g., Hall et al., 2011; Martins et al., 2004), GEM will soon be able to extract inter-particle forces in materials with smaller grains like sands, providing the first chance to validate many theories regarding force networks in natural granular media. GEM will also advance the boundaries of the micro-mechanical understanding of granular materials by offering a characterization tool for a new class of opaque complex assemblies.

Acknowledgments

The authors would like to acknowledge our colleagues in Grenoble, France for fruitful discussions on GEM as a method. Specifically, we would like to acknowledge illuminating discussions with Denis Caillerie and Gioacchino (Cino) Viggiani from Laboratoire 3SR. Also, partial support for this research was provided by the U.S. Department of Defense under AFOSR Center of Excellence award no. FA9550-12-1-0091 and DTRA award no. HDTRA1-12-1-0041. This support is gratefully acknowledged.

References

- Alshibli, K.A., Reed, A.H., 2010. Applications of X-ray Microtomography to Geomaterials, 1st edition Wiley-ISTE.
- Andrade, J., Avila, C., 2012. Granular element method (GEM): linking inter-particle forces with macroscopic loading. *Granular Matter* 14, 51–61.
- Andrade, J.E., Tu, X., 2009. Multiscale framework for behavior prediction in granular media. *Mech. Mater.* 41 (6), 652–669.
- Andrade, J.E., Avila, C.F., Hall, S.A., Lenoir, N., Viggiani, C., 2011. Multiscale modeling and characterization of granular matter: from grain kinematics to continuum mechanics. *J. Mech. Phys. Solids* 59 (2), 237–250.
- Ballard, D.H., 1981. Generalizing the Hough transform to detect arbitrary shapes. *Pattern Recognition* 13 (January (2)), 111–122.
- Bathurst, R.J., Rothenburg, L., 1990. Observations on stress–force–fabric relationships in idealized granular materials. *Mech. Mater.* 9 (1), 65–80.
- Bauer, F., Lukas, M.A., 2011. Comparing parameter choice methods for regularization of ill-posed problems. *Math. Comput. Simulation* 81 (9), 1795–1841.

- Bornert, M., Brémand, F., Doumalin, P., Dupré, J.-C., Fazzini, M., Grédiac, M., Hild, F., Mistou, S., Molimard, J., Orteu, J.-J., Robert, L., Surrel, Y., Vacher, P., Wattrisse, B., 2009. Assessment of digital image correlation measurement errors: methodology and results. *Exp. Mech.* 49, 353–370.
- Bouchaud, J.-P., Claudin, P., Levine, D., Otto, M., 2001. Force chain splitting in granular materials: a mechanism for large-scale pseudo-elastic behaviour. *Eur. Phys. J. E* 4 (4), 451–457.
- Cates, M.E., Wittmer, J.P., Bouchaud, J.-P., Claudin, P., 1998. Jamming, force chains, and fragile matter. *Phys. Rev. Lett.* 81 (August), 1841–1844.
- Christoffersen, J., Mehrabadi, M.M., Nemat-Nasser, S., 1981. A micromechanical description of granular material behavior. *J. Appl. Mech.* 48 (2), 339–344.
- Claudin, P., Bouchaud, J.-P., Cates, M.E., Wittmer, J.P., 1998. Models of stress fluctuations in granular media. *Phys. Rev. E* 57 (April), 4441–4457.
- Coppersmith, S.N., Liu, C.h., Majumdar, S., Narayan, O., Witten, T.A., 1996. Model for force fluctuations in bead packs. *Phys. Rev. E* 53, 4673–4685.
- Correlated Solutions. Vic-2D, Reference Manual.
- Correlated Solutions. Vic-2D, Testing Guide.
- Cundall, P.A., Strack, O.D.L., 1979. A discrete numerical model for granular assemblies. *Géotechnique* 29 (1), 47–65.
- Desrues, J., Viggiani, G., Bésuelle, P. (Eds.), 2006. Advances in X-ray Tomography for Geomaterials. Wiley-ISTE.
- Drescher, A., de Josselin de Jong, G., 1972. Photoelastic verification of a mechanical model for the flow of a granular material. *J. Mech. Phys. Solids* 20, 337–340.
- Frocht, M.M., 1941a. Photoelasticity, vol. 1. Wiley, New York.
- Frocht, M.M., 1941b. Photoelasticity, vol. 2. Wiley, New York.
- Grant, M., Boyd, S., 2011. CVX: Matlab Software for Disciplined Convex Programming, Version 1.21.
- Guo, N., Zhao, J., 2013. The signature of shear-induced anisotropy in granular media. *Comput. Geotech.* 47 (0), 1–15.
- Hall, S., Wright, J., Pirling, T., Andò, E., Hughes, D., Viggiani, G., 2011. Can intergranular force transmission be identified in sand? *Granular Matter* 13, 251–254.
- Hansen, C., 1995. Rank-Deficient and Discrete Ill-Posed Problems. Society for Industrial and Applied Mathematics.
- Howell, D., Behringer, R.P., Veje, C., 1999. Stress fluctuations in a 2d granular couette experiment: a continuous transition. *Phys. Rev. Lett.* 82, 5241–5244.
- Jaeger, H.M., Nagel, S.R., Behringer, R.P., 1996. Granular solids, liquids, and gases. *Rev. Mod. Phys.* 68 (4), 1259–1273.
- Kass, M., Witkin, A., Terzopoulos, D., 1988. Snakes: active contour models. *Int. J. Comput. Vision* 1 (January (4)), 321–331.
- Kroon, D.-J., 2011. Snake: Active contour. <http://www.mathworks.com/matlabcentral/fileexchange>.
- Liu, C.-h., Nagel, S.R., Schecter, D.A., Coppersmith, S.N., Majumdar, S., Narayan, O., Witten, T.A., 1995. Force fluctuations in bead packs. *Science* 269 (523), 513–515.
- Lofberg, J., 2004. Yalmip: a toolbox for modeling and optimization in matlab. In: 2004 IEEE International Symposium on Computer Aided Control Systems Design, pp. 284–289.
- Lötstedt, P., 1983. Perturbation bounds for the linear least squares problem subject to linear inequality constraints. *BIT Numer. Math.* 23, 500–519.
- Majumdar, T.S., Behringer, R.P., 2005. Contact force measurements and stress-induced anisotropy in granular materials. *Nature* 435 (1079), 1079–1082.
- Martins, R.V., Margulies, L., Schmidt, S., Poulsen, H.F., Leffers, T., 2004. Simultaneous measurement of the strain tensor of 10 individual grains embedded in an al tensile sample. *Mater. Sci. Eng. A* 387–389 (0), 84–88. (13th International Conference on the Strength of Materials).
- Ostojic, S., Somfai, E., Nienhuis, B., 2006. Scale invariance and universality of force networks in static granular matter. *Nature* 439 (7078), 828–830.
- Pan, B., Qian, K., Xie, H., Asundi, A., 2009. Two-dimensional digital image correlation for in-plane displacement and strain measurement: a review. *Meas. Sci. Technol.* 20 (6), 062001.
- Peng, T., 2010. Detect circles with various radii in grayscale image via hough transform. <http://www.mathworks.com/matlabcentral/fileexchange>.
- Peters, J.F., Muthuswamy, M., Wibowo, J., Tordesillas, A., 2005. Characterization of force chains in granular material. *Phys. Rev. E* 72 (October), 041307.
- Poulsen, H.F., 2004. Three-Dimensional X-Ray Diffraction Microscopy: Mapping Polycrystals and their Dynamics. Springer, New York.
- Radjai, F., Jean, M., Moreau, J.J., Roux, S., 1996. Force distributions in dense two-dimensional granular systems. *Phys. Rev. Lett.* 77 (July), 274–277.
- Radjai, F., Wolf, D.E., Jean, M., Moreau, J.J., 1998. Bimodal character of stress transmission in granular packings. *Phys. Rev. Lett.* 80 (1), 61–64.
- Rothenburg, L., Bathurst, R.J., 1989. Analytical study of induced anisotropy in idealized granular materials. *Géotechnique* 39 (4), 601–614.
- Saadatfar, M., Sheppard, A.P., Senden, T.J., Kabla, A.J., 2012. Mapping forces in a 3d elastic assembly of grains. *J. Mech. Phys. Solids* 60 (1), 55–66.
- Santamarina, J.C., Klein, K.A., Fam, Moheb A., 2001. Soils and Waves. John Wiley & Sons.
- Satake, M., 1982. Fabric tensor in granular materials. In: Vermeer, P.A., Luger, H.J. (Eds.), Deformation and Failure of Granular Materials, pp. 63–68.
- Sturm, J.F., 1999. Using sedumi 1.02, a MATLAB toolbox for optimization over symmetric cones. *Optim. Methods Software* 11–12, 625–653.
- Sutton, M.A., Orteu, J.J., Schreier, H., 2009. Image Correlation for Shape, Motion and Deformation Measurements: Basic Concepts, Theory and Applications. Springer.
- Vlahinic, I., Andò, E., Viggiani, G., Andrade, J.E., Towards a more accurate characterization of granular media: extracting quantitative descriptors from grain-scale images. *Granular Matter*, under review.
- Vogel, C.R., 2002. Computational Methods for Inverse Problems. Society for Industrial and Applied Mathematics.
- Wang, J.Y., Park, L., Fu, Y., 2007. Representation of real particles for DEM simulation using x-ray tomography. *Constr. Build. Mater.* 21 (2), 338–346.
- Zhou, J., Long, S., Wang, Q., Dinsmore, A.D., 2006. Measurement of forces inside a three-dimensional pile of frictionless droplets. *Science* 312 (5780), 1631–1633.